

UNITSIM-Galaxies: data release and clustering of emission-line galaxies

Alexander Knebe,^{1,2,3*} Daniel Lopez-Cano,^{1,9} Santiago Avila,^{1,4} Ginevra Favole,⁵

Adam R. H. Stevens,³ Violeta Gonzalez-Perez,^{1,2} Guillermo Reyes-Peraza,^{1,4}

Gustavo Yepes,^{1,2} Chia-Hsun Chuang,⁶ Francisco-Shu Kitaura^{7,8}

¹*Departamento de Física Teórica, Módulo 15, Facultad de Ciencias, Universidad Autónoma de Madrid, 28049 Madrid, Spain*

²*Centro de Investigación Avanzada en Física Fundamental (CIAFF), Facultad de Ciencias, Universidad Autónoma de Madrid, 28049 Madrid, Spain*

³*International Centre for Radio Astronomy Research, University of Western Australia, 35 Stirling Highway, Crawley, Western Australia 6009, Australia*

⁴*Instituto de Física Teórica, (UAM/CSIC), Universidad Autónoma de Madrid, Cantoblanco, E-28049 Madrid, Spain*

⁵*Institute of Physics, Laboratory of Astrophysics, Ecole Polytechnique Fédérale de Lausanne (EPFL), Observatoire de Sauverny, 1290 Versoix, Switzerland*

⁶*Kavli Institute for Particle Astrophysics and Cosmology, Stanford University, 452 Lomita Mall, Stanford, CA 94305*

⁷*Instituto de Astrofísica de Canarias (IAC), Calle Vía Lactea s/n, 38200, La Laguna, Tenerife, Spain*

⁸*Departamento de Astrofísica, Universidad de La Laguna (ULL), E-38206, La Laguna, Tenerife, Spain*

⁹*Donostia International Physics Center (DIPC), Paseo Manuel de Lardizabal, 4, 20018 Donostia-San Sebastián, Spain*

Last updated 2015 May 22; in original form 2013 September 5

ABSTRACT

New surveys such as ESA’s Euclid mission and NASA’s Nancy Grace Roman Space Telescope are planned to map with unprecedented precision the large-scale structure of the Universe by measuring the 3D positions of tens of millions of galaxies. It is necessary to develop theoretically modelled galaxy catalogues to estimate the expected performance and to optimise the analysis strategy of these surveys. We populate two pairs of $(1h^{-1}\text{Gpc})^3$ volume dark-matter-only simulations from the UNIT project with galaxies using the SAGE semi-analytic model of galaxy formation, coupled to the photoionisation model `GET_EMLINES` to estimate their $H\alpha$ emission. These catalogues represent a unique suite that includes galaxy formation physics and – thanks to the fixed-pair technique used – an effective volume of $\sim (5h^{-1}\text{Gpc})^3$, which is several times larger than the Euclid survey. We study the abundance and clustering of those model star-forming $H\alpha$ emission-line galaxies (ELGs). For scales greater than $\sim 5h^{-1}\text{Mpc}$, we find for the ELGs a scale-independent bias with values in the range $b \in [1, 4.5]$, increasing with redshift over the interval $z \in [0.5, 2]$. Model galaxy properties, including their emission-line fluxes are publicly available.

Key words: methods: numerical – galaxies: formation – galaxies: high-redshift – galaxies: abundances – cosmology: theory – large-scale structure of the universe

1 INTRODUCTION

During the last few decades, numerous projects have been aimed at creating large cartographic maps of galaxies, such as 2dFGRS (Cole et al. 2005), SDSS (York et al. 2000; Eisenstein et al. 2005), WiggleZ (Drinkwater et al. 2010; Parkinson et al. 2012), BOSS (Dawson et al. 2012; Alam et al. 2017), eBOSS (Dawson et al. 2016; eBOSS Collaboration et al. 2020) or DES (The Dark Energy Survey Collaboration 2005; Abbott et al. 2018). They have been carried out with the objective of trying to better understand the large-scale structure of the Universe, to estimate the different parameters that regulate the formation of structures, to determine the expansion history of the Universe, to study how galaxies form, to reconstruct their star formation histories, and to impose constraints upon different models that currently exist for dark energy and for alternative theories of gravity. While advances have certainly been made, all these grand topics remain open areas of investigation, and likely will for years to come.

New surveys such as Euclid (Laureijs et al. 2011; Amendola et al.

2013), the Nancy Grace Roman Space Telescope (Spergel et al. 2013, 2015), the Dark Energy Spectroscopic Instrument (DESI, Collaboration et al. 2016), and the 4-metre Multi-Object Spectroscopic Telescope (4MOST, de Jong et al. 2012) are planned to map with unprecedented precision the large-scale structure of the Universe by measuring the 3D positions of tens of millions of galaxies. These missions are expected to start operating in the coming years, providing the scientific community with wider, deeper, and more accurate data, which may be used to impose stronger constraints upon theoretical models and to provide more accurate estimates for some of the aforementioned parameters relevant in cosmology. Some of these forthcoming missions (e.g., Euclid) will focus on conducting spectroscopic surveys of galaxies using near-infrared grisms in order to determine the positions of galaxies by observing their emission lines such as $H\alpha$. The wavelength of the observed emission lines will serve to determine the redshifts corresponding to the detected objects.

Observational campaigns need to be complemented by cosmological simulations: a cornerstone of large-scale structure analysis. They are used to inform and validate galaxy clustering models, to test and optimise different estimators and analysis pipelines, to estimate covariance matrices, and to compare with measurements from

* Contact e-mail: alexander.knebe@uam.es

data. Whereas the smaller scales are known to contain many more Fourier modes and hence constraining power, it is also known that they are heavily affected by the physics of galaxy formation. But since the spatial volumes that the aforementioned surveys seek to study is notoriously large, it is still necessary to rely on dark-matter-only simulations in which galaxies are introduced in post-processing either by halo occupation distribution (HOD, e.g. Berlind et al. 2003, as well as the *Euclid Flagship mock galaxy catalogue*), (sub-)halo abundance matching (SHAM, e.g. Vale & Ostriker 2004) or semi-analytic models (SAM) (e.g. the MultiDark-Galaxies,¹ Knebe et al. 2018a). While there are efforts to push the limits of ‘full physics’ hydrodynamical simulations to larger and larger volumes (e.g. Lee et al. 2020), it still remains more feasible to match the volumes that missions like Euclid will cover with gravity-only simulations.

The demand for large volumes modelled with sufficiently high resolution is also the reason why, during the last years, alternatives to running such demanding simulations have been explored. For instance, the technique developed by Angulo & Pontzen (2016) dramatically reduces the variance arising from the sparse sampling of wavemodes in cosmological simulations. The method uses two simulations that are ‘fixed’ and ‘paired’, i.e. the initial Fourier mode amplitudes are fixed to the ensemble average power spectrum and their phases are shifted by π . This approach has been adopted by the UNIT collaboration² (Chuang et al. 2019) where it has been shown that the effective volume of such fixed-and-paired simulations can be several times larger than the actual volume simulated: in Chuang et al. (2019) we have shown that the original four $(1h^{-1}\text{Gpc})^3$ simulations correspond to a total effective volume of ca. $(5h^{-1}\text{Gpc})^3$, i.e. ~ 7 times of the survey volume of Euclid or DESI. We use the same two pairs of simulations for our study here, too. Our simulations simultaneously include the large scales with an accuracy greater than expected by these surveys, and have been passed through a post-processing that models the relevant physics. In terms of galaxy clustering statistics, each pair can be as precise on (non-)linear scales as an average over approximately 150 traditional simulations. They therefore are suitable to statistically study matter–galaxy interplay and galaxy clustering alongside its bias.

In this work we present and use galaxy catalogues for simulations that were generated by applying the SAGE semi-analytic model (Croton et al. 2016) to the aforementioned gravity-only UNIT simulations. The resulting galaxies have further been processed with the GET_EMLINES code (Orsi et al. 2014) in order to obtain emission-line properties for star-forming galaxies. From previous observational studies (Sobral et al. 2016), it is expected that over 80% of the emission-line galaxies observed by Euclid will be star-forming galaxies, and hence our approach to model only star-forming emission-line galaxies is adequate for this study. Using these catalogues, we study the predicted abundance of H α emitters as a function of flux and redshift and compare it with observational data. For our reference model, we impose a flux limit of 2×10^{-16} erg/s/cm² in the redshift range $0.9 < z < 1.8$, corresponding to Euclid’s specifications. We construct two additional models whose number densities of ELGs has been adjusted to the models #1 and #3 of Pozzetti et al. (2016, from now on P16). We also study the clustering of our H α galaxies and their bias with respect to the dark matter field. The bias is a key parameter and a result of not only halo formation but also the varied physics of galaxy formation that can cause the spatial distribution

of baryons to differ from that of dark matter. The bias connects the observed statistics to theoretical predictions. Our reported quantities may be used to make forecasts for Euclid and related studies for which both the abundance and bias of H α ELGs is an input.

There exist previous works based upon emission-line galaxies modelled in the UNIT simulations (Zhai et al. 2021; Zhai et al. 2019). However, the important difference to our work is that in those papers only one of the UNIT simulations has been used (as opposed to all four here). Zhai et al. also applied a completely different modelling for the ELGs, namely the GALACTICUS semi-analytic model coupled to the CLOUDY photoionisation code (Ferland et al. 2013) for the calculation of emission line properties. Further, their SAM was calibrated using observations of the H α luminosity function in the redshift range $z \in [0.8, 2.3]$, whereas for our SAGE catalogues this will be a clear prediction. And while Zhai et al. also studied galaxy clustering in the later work, they have not investigated the bias. Our work therefore extends those previous studies and should be viewed as complementary. We further make the four independent galaxy catalogues publicly available.

The structure of this article is as follows. In Section 2 the methods used to generate the ELG catalogues are presented, namely the N -body UNIT simulations (Section 2.1), the SAGE semi-analytic model (Section 2.2) and the emission-line modelling (Section 2.3). Next, in Section 3, we present a series of figures to validate the galaxy catalogues generated by SAGE by comparing key properties with observational results. Then in Section 4 we examine the validity of the modelling for the emission lines of the galaxies. Afterwards, in Section 5, the results obtained by studying the two-point correlation function and the bias obtained for the ELGs in the Euclid range of redshifts will be presented. Finally, in Section 6, the conclusions derived from this work will be outlined.

2 THE METHODS

2.1 The UNIT Simulations

As a basis for this work, four gravity-only simulations that have been developed within the UNIT project have been employed. The names for the two pairs of simulations that we use throughout this work are UNITSIM1 (U1), UNITSIM1-Inverted Phase (U1IP), UNITSIM2 (U2), and UNITSIM2-Inverted Phase (U2IP). The procedure followed for generating these simulations as well as an analysis of the resulting correlation properties is discussed in Chuang et al. (2019). For this particular study we have used the two pairs of simulations in which the code GADGET (Springel et al. 2001) has been used to study the behavior of a total of 4096^3 particles in a volume of $1h^{-3}\text{Gpc}^3$ per simulation, thus obtaining a mass resolution of $1.2 \times 10^9 h^{-1}M_{\odot}$ per simulation particle.

In Chuang et al. (2019) it is also explained how the ROCKSTAR halo catalogues and the corresponding CONSISTENTTREES merger trees have been generated for each of the gravity-only simulations using the publicly available codes from Behroozi et al. (2012). All the data corresponding to the UNIT simulations (incl. the galaxy and ELG catalogues presented here) are publicly available at <http://www.unitsims.org>. By making the galaxy catalogues and their emission-line properties available too, this work further adds to the community.

¹ Galaxy catalogues based upon three distinct SAMs can be downloaded from CosmoSim.

² <http://www.unitsims.org>

2.2 Semi-analytic galaxy modelling via SAGE

SAGE (Semi-Analytic Galaxy Evolution, Croton et al. 2016) is a modular, publicly available³ semi-analytic model of galaxy formation, branched from the Munich family of models (specifically from Croton et al. 2006). Haloes (in this case, from the UNIT simulations) are initially seeded with ‘hot’ gas based on the cosmic baryon fraction (modulo a reionization factor at higher redshift and in low-mass haloes). Cooling/accretion of this gas onto the central galaxy is based on the two-mode (hot and cold) model of White & Frenk (1991). Star formation in the disk occurs once the gas is above a critical average surface density (see Kennicutt 1989; Kauffmann 1996). Metals are immediately injected and gas recycled into the inter-stellar medium (ISM), where a constant mass-loading factor is also applied to reheat gas out of the disk, some of which will end up in an ejected component if the energy budget allows it. A parametrized fraction of the ejected gas (connected to the virial velocity) is reincorporated into the halo on a dynamical time-scale. Satellite galaxies are tracked in the merger trees until merged or unresolved. Once their subhaloes become unresolved, satellites are either disrupted (where their baryons are placed in intracluster reservoirs) or immediately merged with the central. SAGE, therefore, does not have orphan galaxies. Mergers and disk instabilities trigger starbursts, drive stars into the bulge, and cause gas to be accreted onto the central black hole. This triggers quasar-mode active galactic nuclei (AGN) feedback, which reheats gas from the disk. When galaxies have sufficiently (super)massive black holes, cooling is also suppressed by radio-mode AGN activity (both past and present), modelled by a phenomenological ‘heating’ radius that can only grow with time, within which gas cannot cool.

This is the same SAGE model that was also applied to the MultiDark simulation MDPL2 (Knebe et al. 2018a) and no further re-calibration has been deemed necessary. The model was calibrated for that simulation by fitting visually first the $z = 0$ stellar mass function (Baldry et al. 2008), and secondarily using the stellar metallicity–mass relation (Tremonti et al. 2004), baryonic Tully–Fisher relation (Stark et al. 2009), black hole–bulge mass relation (Scott et al. 2013), and cosmic star formation rate density (Somerville et al. 2001). The model has not been re-calibrated here as both the UNIT and MDPL2 simulations were run with the same cosmological parameters (Planck Collaboration et al. 2015) and have the same box size. However, the mass resolution is marginally better for UNITSIM, due to the 20 per cent larger number of particles. For the general performance of the SAGE model we refer the reader to the results presented in Knebe et al. (2018a), as the calibration plots change minimally when going from MDPL2 to UNIT (see also Fig. 1, in this paper). The calibration does not include constraints for emission-line galaxies.

For a more detailed description of the model we refer the reader to Croton et al. (2016) and section 2.4 of Knebe et al. (2018a).

2.3 Emission-line galaxy modelling

Once we have populated the dark matter haloes from the UNIT simulations with the semi-analytic galaxies generated by SAGE we obtain values for the intensity of the most relevant emission lines such as $H\alpha$, [OIII]4959, [OIII]5007, [NII]6548 and [NII]6584 for each of the model galaxies. In this study we focus on the $H\alpha$ line, leaving the other emission lines for future work.

GET_EMLINES code. In order to reproduce the intensity of $H\alpha$ emission lines of our galaxies, we have used the method presented in Orsi et al. (2014), i.e. the publicly available GET_EMLINES code.⁴ This code is based on the algorithm MAPPINGS-III described in Groves et al. (2004) and Allen et al. (2008), which relates the ionization parameter of gas in galaxies, q , to their cold-gas metallicity Z_{cold} as:

$$q(Z) = q_0 \left(\frac{Z_{\text{cold}}}{Z_0} \right)^{-\gamma}, \quad (1)$$

where q_0 is the ionisation parameter of a galaxy that has cold gas metallicity Z_0 and γ is the exponent of the power law. We adopted the suggested values of $q_0 = 2.8 \times 10^7 \text{ cm s}^{-1}$ and $\gamma = 1.3$, which were found to yield $H\alpha$ luminosities for star-forming galaxies in good agreement with observations (Orsi et al. 2014). Cold gas metallicity is defined as the ratio between the cold gas mass in metals to the total cold-gas mass:

$$Z_{\text{cold}} = \frac{M_{Z,\text{cold}}}{M_{\text{cold}}}. \quad (2)$$

The other relevant component is the star formation rate (SFR).⁵ Note that SAGE provides this quantity averaged over the last time-step. But the model ideally requires as inputs the instantaneous SFR and cold gas metallicity of galaxies. However, Favole et al. (2019) have shown that for galaxies that are not too bright the differences are negligible. To be able to properly compare our results to observations we convert the luminosities to fluxes and also apply a dust extinction to the luminosities of the model galaxies. As the code requires the star-formation rate as an input, our model galaxies should be considered ‘star-forming’.

Dust extinction. The particular dust model used is described in great detail in Favole et al. (2019)⁶, but we also summarize it here. The attenuation from interstellar dust is added to the intrinsic $H\alpha$ luminosity using:

$$L(\lambda_j)^{\text{att}} = L(\lambda_j)^{\text{intr}} 10^{-0.4A_\lambda(\tau_\lambda^z, \theta)}, \quad (3)$$

where the attenuation coefficient, as a function of the galaxy optical depth τ_λ^z and the dust scattering angle θ , is defined as (Osterbrock 1989; Draine 2003; Izquierdo-Villalba et al. 2019; Favole et al. 2019):

$$A_\lambda(\tau_\lambda^z, \theta) = -2.5 \log_{10} \frac{1 - \exp(-a_\lambda \sec \theta)}{a_\lambda \sec \theta}. \quad (4)$$

In Eq. (4), $a_\lambda = \sqrt{1 - \omega_\lambda} \tau_\lambda^z$, and ω_λ is the dust albedo. We assume $\cos \theta = 0.30$ and $\omega_\lambda = 0.56$, meaning that the scattering is not isotropic but forward-oriented, and about 60% of the extinction is caused by scattering.

The galaxy optical depth is defined as (Hatton et al. 2003; De Lucia & Blaizot 2007):

$$\tau_\lambda^z = \left(\frac{A_\lambda}{A_V} \right)_{Z_\odot} \left(\frac{Z_{\text{cold}}}{Z_\odot} \right)^{1.6} \left(\frac{\langle N_H \rangle}{2.1 \times 10^{21} \text{ atoms cm}^{-2}} \right), \quad (5)$$

in terms of the cold gas metallicity Z_{cold} defined in Eq. (2) and the extinction curve for solar metallicity, which we take to be that of the

³ <https://github.com/darrencroton/sage>

⁴ https://github.com/aaorsi/get_emlines

⁵ Total SFR in SAGE is the sum of the SfrDisk and SfrBulge fields.

⁶ <https://github.com/gfavole/dust>

Sun: $Z_{\odot} = 0.0134$ (Asplund et al. 2009). We assume the Cardelli et al. (1989) extinction law:

$$\left(\frac{A_{\lambda}}{A_V}\right) = a(x) + b(x)/R_V, \quad (6)$$

where $x \equiv \lambda^{-1}$, $R_V \equiv A_V/E(B-V) = 3.1$ is the ratio of total to selective extinction for the diffuse interstellar medium in the Milky Way, and

$$\begin{aligned} a(x) &= 1 + 0.17699y - 0.50447y^2 - 0.02427y^3 + \\ &\quad 0.72085y^4 + 0.01979y^5 - 0.77530y^6 + 0.32999y^7, \\ b(x) &= 1.41338y + 2.28305y^2 + 1.07233y^3 - 5.38434y^4 \\ &\quad - 0.62251y^5 + 5.30260y^6 - 2.09002y^7, \end{aligned} \quad (7)$$

with $y = (x - 1.82)$. The quantity $\langle N_H \rangle$ in Eq. (5) is the mean hydrogen column density defined as (Hatton et al. 2003; De Lucia & Blaizot 2007):

$$\langle N_H \rangle = \frac{M_{\text{cold}}^{\text{disk}}}{1.4 m_p \pi (R_{1/2}^{\text{disk}})^2} \text{ atoms cm}^{-2}, \quad (8)$$

where $M_{\text{cold}}^{\text{disk}}$ is the cold-gas mass of the disk, $m_p = 1.67 \times 10^{-27}$ kg is the proton mass, and $R_{1/2}^{\text{disk}}$ is the half-mass radius of the disk.

We caution that emission lines are expected to be more attenuated than the continuum, e.g. De Barros et al. (2016), which is the model used here.

3 THE SAGE GALAXIES

The aim of this section is to validate how well our theoretically modelled SAGE galaxies perform with respect to the quantities that enter into the calculation of the emission-line properties. This involves a) stellar mass, b) star formation rates, c) metallicities, and d) disk lengths. We will further focus on redshifts in the range $z \in [1, 2]$ and compare to observational data where possible. For comparisons of other properties to observations and the calibration plots, respectively, we refer the reader to Knebe et al. (2018a) where it had been applied to the MultiDark simulation MDPL2.

3.1 Stellar Mass Function

The stellar mass function (SMF) is one of the most significant properties that can be inferred from galaxy surveys since this function represents the number of galaxies normalized to the volume of the survey/simulation and to the bin width. Its simplicity yet fundamental importance means the SMF is often employed for calibrating semi-analytic models such as SAGE used here.

In the main panel of Fig. 1 the results obtained for the SMF computed from the SAGE galaxies modelled over the UNITSIM1 simulation are presented for three different redshifts $z = [0.0, 1.710, 2.695]$. Together with the results obtained from our simulation, a series of observational results obtained for a range of redshifts similar to those simulated are also represented in the same figure. The compilation for redshift $z = 0$ is taken from the so-called ‘CARNage calibration’ data set described in great detail in section 3.3 and appendix A of Knebe et al. (2018b)⁷. The observations for the higher redshifts are taken from Davidzon et al. (2017) and are based on the UltraVISTA

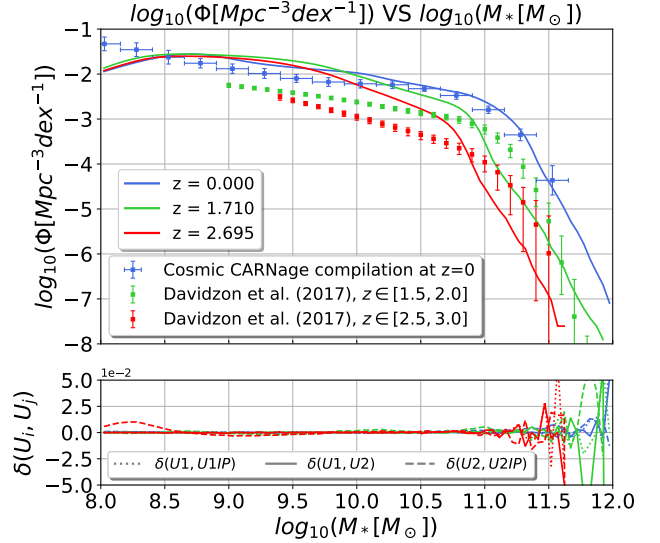


Figure 1. Stellar mass function. In the upper panel we compare the results for the modelled galaxies at various redshifts (solid lines) to observational data (points with error bars). The lower panel shows the fractional difference of U1 to the other UNIT simulations. Note that the $z = 0$ SMF has been used to calibrate the SAGE model whereas the results for higher redshift are a prediction of the model.

near-infrared survey of the COSMOS field. In the bottom panel of Fig. 1 the variation in SMF between U1 and the three other UNIT simulations is shown, i.e. the y-axis represents⁸

$$\delta(U_i, U_j) = \frac{\text{SMF}(U_i)}{\text{SMF}(U_j)} - 1. \quad (9)$$

For all the simulations conducted, the results produced for the SMF qualitatively follow the observational trends. This outcome is in line with previous results such as those presented in Favole et al. (2019) and Asquith et al. (2018). The results obtained at redshift $z = 0$ agree almost seamlessly with the observational data. This is readily explained by the fact that the SAGE model was pre-calibrated to very similar data. When studying the behavior at higher redshifts (which is a prediction of the model) certain discrepancies start to show up. For stellar masses below $10^{11} M_{\odot}$ the SMF calculated for the SAGE galaxies exceeds the observational points, while the opposite is true for masses higher than $10^{11} M_{\odot}$. This is related to the condition that getting both the SMF at $z = 0$ and the cosmic star-formation history to simultaneously agree with the observations demands to model stars that should have been formed in haloes below this simulation’s resolution limit. This inevitably leads to resolved high- z galaxies having too much stellar mass (and star-formation rates that are too high) in the model. It also changes how galaxies acquire stellar mass through mergers (as fewer mergers are resolved), which might help explain why there are too few galaxies with $M_* > 10^{11} h^{-1} M_{\odot}$ at higher z in the model. Additionally, the deviations observed here for high redshifts – especially at the low-mass end – are similarly found when studying the SMF produced by other semi-analytic models, as extensively discussed in Asquith et al. (2018). Our explanation is hence generic and not only applies to SAGE. Therefore, despite the discrepancies seen in Fig. 1, the results obtained are reasonably accurate for us to say that the modelled SAGE galaxies fairly depict

⁷ The ‘CARNage calibration’ set is available for download from <http://popia.ft.uam.es/public/CARNageSet.zip>.

⁸ Note that we use the same strategy for presenting the variations across the four UNIT simulations in practically all plots.

the behaviour of the SMF that could be expected in the redshift range for which Euclid is expected to operate.

Another important aspect worth mentioning in this section is that due to resolution limitations in our simulations, galaxies whose stellar mass is lower than $10^9 M_\odot$ have not been considered. Please refer to Knebe et al. (2018b,a) for a justification of this threshold, but we can also see in Fig. 1 how the number of galaxies starts to decline for stellar masses below that threshold due to numerical limitations. Therefore, to produce the results presented in the following sections we will discard all those galaxies whose mass is inferior to this threshold. This is not a cause for concern in this work though, as the vast majority of relevant ELGs have stellar masses above this threshold (see Appendix A1).

3.2 Star Formation

With respect to the star formation (SF) in galaxies, which is also used as an input to the GET_EMLINES code, we only present the relation between specific star formation (i.e. SF per unit stellar mass) and stellar mass at redshift $z \sim 2$. We find that SAGE makes a prediction for this relation that is in excellent agreement with the observations of Daddi et al. (2007): in the main panel of Fig. 2 the specific SF rate (sSFR) of U1-SAGE galaxies is plotted against the stellar mass M_* for redshift $z = 2.028$. We show both the contours of a 2D histogram of this scatter plot as well as the median of the values obtained for sSFR within a series of bins along the x -axis. As is customary, in the bottom panel of the Fig. 2 the variations between simulations with respect to the other UNITSIM-SAGE galaxies have been represented. We further compare our model results to observational data extracted from Daddi et al. (2007), which appears to be in agreement with the results found in our simulation, at least within the $1 - \sigma$ regions. Though not explicitly shown here, we also confirm that our SAGE results are in excellent agreement with observational data for the sSFR (as provided by Elbaz et al. 2011) as a function of stellar mass at redshift $z = 0$. These results, in turn, are also compatible to those shown in Favole et al. (2019) for redshift $z = 0.1$.

For a comparison of the star formation rate (SFR) function to observational data at redshift $z = 0.14$ and the redshift evolution of the cosmic star formation rate density, we refer the reader to Knebe et al. (2018a). While the SFR function is compatible with the observational data at low redshift – as seen for the MultiDark galaxies and also confirmed for the UNITSIM galaxies (though not explicitly presented here) – it is worth mentioning that for SFR values greater than $\sim 10^{1.6} M_\odot/\text{yr}$, the number of galaxies generated with SAGE seems to underestimate the observed number (see fig. 2 in Knebe et al. 2018a). As we will see later in Section 4.1 this is going to leave an imprint on the abundance of ELGs, especially at high redshifts. We finally like to remark that the relation between specific SFR and stellar mass as shown here is a prediction of the SAGE model.

Based on these results, we can say that our galaxies sufficiently reproduce the behaviour of the sSFR that would be expected for a sample of real galaxies in Euclid’s operating range of redshifts.

3.3 The mass-metallicity relation

Another aspect of galaxies to be considered for the emission-line modelling is the chemical composition, since – depending on the fraction of metals that a galaxy may contain – its SFR may be substantially modified due to the fact that a higher metal content favours cooling mechanisms. This property is explicitly taken into account by the GET_EMLINES code and has to be provided as an input, respectively.

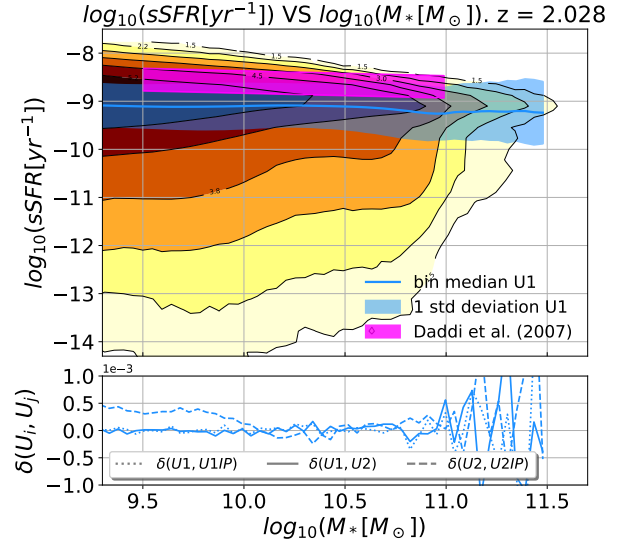


Figure 2. Specific star formation rate vs. stellar mass at redshift $z \sim 2$ in comparison to observations by Daddi et al. (2007). We show both the median (solid blue line) and the contour levels of the scatter relation. This relation is a prediction of the SAGE model.

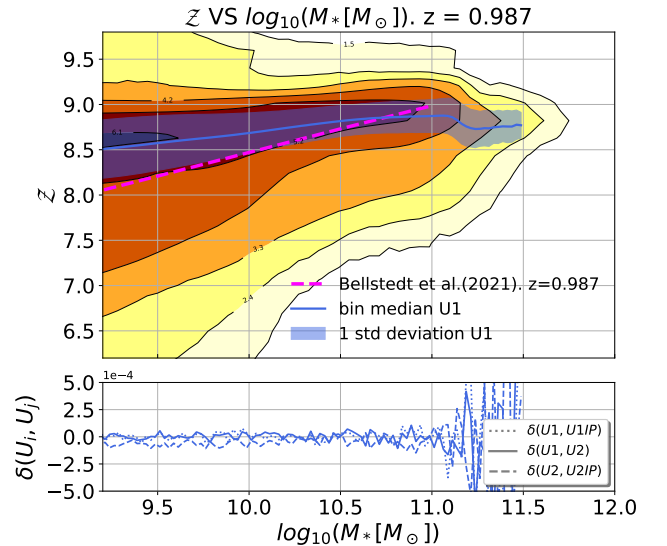


Figure 3. Cold gas metallicity vs. stellar mass. The relation shown here for redshift $z \sim 1$ is a prediction of the SAGE model. We also show the relation as found in Bellstedt et al. (2021) (dashed line).

Since SF is regulated by the collapse of cold gas clouds, in Fig. 3 we study the relation that exists between the total mass of metals contained in such clouds and the total mass of cold gas in a given galaxy throughout the parameter Z which is calculated as (Favole et al. 2019; Knebe et al. 2018a):

$$Z = 8.69 + \log_{10} Z_{\text{cold}} - \log_{10} 0.02 \quad (10)$$

where Z_{cold} was previously defined in Eq. (2). Note that this quantity Z is meant to be a proxy for $12 + \log(\text{O}/\text{H})$.

In the main panel of Fig. 3 we show the correlation between Z and stellar mass as contours alongside the median (solid blue line) for redshift $z \sim 1$. The lower panel shows again the fractional difference

with respect to the other UNITSIM model. The relation is as expected, i.e. larger mass galaxies have larger metallicities, with a strength comparable to the one observed for lower redshifts. This relation – as observed at redshift ~ 0.1 – is used during the calibration of the SAGE model; its extension to $z \sim 1$ shown here nevertheless is a clear prediction. We also show the relation as expected from observations by using the best-fit function presented in [Bellstedt et al. \(2021, eq. 6 in there\)](#). This fitting function was obtained by applying the spectral-energy-distribution-fitting code ProSpect to galaxies from the Galaxy and Mass Assembly (GAMA) survey at $z < 0.06$; comparing with observations of gas-phase metallicity over a large range of redshifts, they then showed that their best-fit evolving mass–metallicity relationship is consistent with observations at all epochs and hence used here by us at redshift $z \sim 1$. We only show the Bellstedt et al. function out to $M_* = 10^{11} M_\odot$ which was their limit for obtaining the best-fit parameters. The predictions of the SAGE model are in fair agreement with the Bellstedt et al. function. If one were to extrapolate the Bellstedt results, we would find a deficit of cold gas metallicity for the highest mass galaxies with $M_* > 10^{11} M_\odot$. Even though there is no observational data in that regime, one possible explanation could be that the cold gas in those galaxies comes from mergers rather than accretion/cooling. I.e. AGN feedback might have shut off cooling entirely, so enriched gas in the circumgalactic medium will not get back to the inter-stellar medium. Instead, we might just be seeing the low-metallicity gas from now-cannibalised low-mass galaxies dominating most of the cold gas in the galaxy. But it yet remains unclear if the drop in metallicity predicted for SAGE galaxies at $M_* = 10^{11} M_\odot$ will also be seen in observations.

3.4 The disk size–mass relation

The last relevant quantity to validate for our SAGE galaxies is the size of the disk. While it is not relevant for GET_EMLINES it nevertheless enters into the dust attenuation model via Eq. (8). We therefore show in Fig. 4 the correlation of the effective disk radius (as calculated by SAGE) with stellar mass at redshift $z = 1.22$. For comparison we use the best-fit relation as reported by [Yang et al. \(2021, eq. 1\)](#) for late-type galaxies at redshift $z = 1.25$ and as derived from the complete Hubble Frontier Fields data set. While the agreement is very good for higher mass galaxies, the disks sizes predicted by SAGE for galaxies with mass $M_* < 10^{10} M_\odot$ are up to a factor of three larger than observed. However, this is not really affecting our results here as our ELGs preferentially have stellar masses $M_* > 10^{10.5} M_\odot$ (see Fig. A1).

Given all the results presented throughout this particular section, with the majority even being predictions of the SAGE model, we are confident that our UNITSIM-SAGE galaxies meet all the requirements to be used for the emission-line modelling which is discussed in great detail in the following Section.

4 SAGE'S EMISSION-LINE GALAXIES (ELGS)

The results presented in the previous section indicate that our model galaxies are in reasonable agreement with a range of observations, especially those properties that are used to model emission-line galaxies. Here we now contrast the properties of our simulated star-forming ELGs with a set of observations, too. Note, the ELGs are by construction a subset of the full SAGE catalogue.

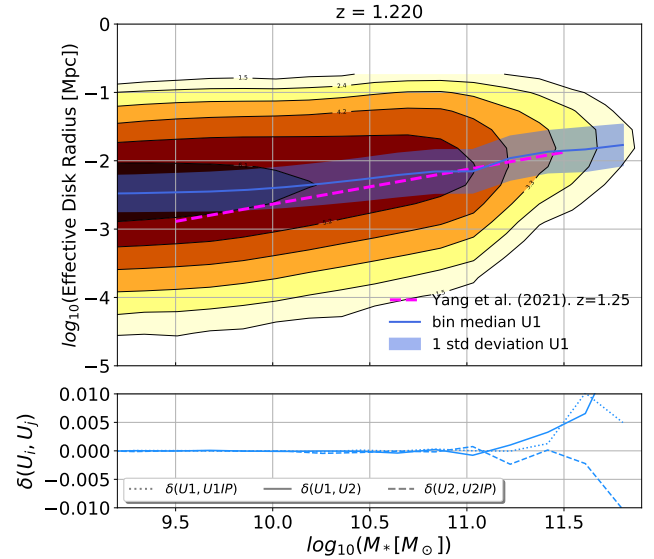


Figure 4. Effective disk radius as a function of stellar mass (contours and blue solid line with 1σ error region). This is a prediction of the SAGE model. We also show the relation as reported for late-type galaxies in [Yang et al. \(2021\)](#) at $z = 1.25$ (dashed line).

4.1 Abundance of H α -ELGs

The model presented in Section 2.3 provides us with the relevant luminosities in – amongst other lines – H α for all our SAGE galaxies. However, when comparing them to observations at a particular redshift they were converted to fluxes as well as being passed through an appropriate dust attenuation model (see Section 2.3). To verify the credibility of our (attenuated) ELGs we study in Fig. 5 the (cumulative) distribution functions of the number of ELGs per deg^2 as a function of H α flux for various redshifts in the range $z \in [1, 2]$.⁹ The solid lines show the original fluxes whereas the dashed lines are based upon fluxes after applying our dust model. We decided to only show the results for U1 as the other three ELG catalogues give indistinguishable results (and therefore also omit the usual variation plot). As is the case for all plots, only galaxies with stellar mass greater than $10^9 M_\odot$ have been considered. The data points in both panels are observations taken from [Colbert et al. \(2013, Table 2\)](#). While it is obvious how the dust model shifts the contribution to the cumulative number counts towards lower fluxes (and into better agreement with observations), we also find that our model ELGs lack objects with high fluxes. We attribute this to aforementioned deficiency of galaxies with high star-formation rate (not explicitly shown here, but please refer to fig. 2 in [Knebe et al. 2018a](#)). In any case, we observe that with decreasing redshift the number of ELGs for a given flux threshold increases – something we quantify better in the following sub-section.

4.2 Abundance evolution of flux-selected H α -ELGs

Throughout the remainder of the paper we will primarily focus on the attenuated fluxes and apply lower limits to them. Our reference flux threshold is $F_{\text{cut}} = 2 \times 10^{-16} \text{ erg/s/cm}^2$ across all redshifts, which corresponds to the limit of the Euclid satellite. We refer to

⁹ The conversion from number of galaxies per volume to dN/dz in $[\text{gal}/\text{deg}^2]$ is presented in Appendix B.

Table 1. The two columns for the reference model RefMod list the average number density of ELGs per square degree (dN/dz) and its standard deviation when applying a redshift-independent flux cut of 2×10^{-16} erg/s/cm² to our dust-attenuated star-forming ELGs. The two columns for each of our models PozMod1 and PozMod3 give the predicted number density of ELGs per square degree (taken from their Table 3) and the flux threshold (measured in 10^{-16} erg/s/cm²) required to match that number for our SAGE ELGs, as an average over all four UNIT simulations (the standard deviation is smaller than the reported accuracy).

z	RefMod ($F_{\text{cut}} = 2$)		PozMod1		PozMod3	
	$\langle dN/dz \rangle$	σ	dN/dz	$\langle F_{\text{cut}} \rangle$	dN/dz	$\langle F_{\text{cut}} \rangle$
0.490	15262	30	9946	2.85	–	–
0.987	3238	12	7353	1.37	3779	1.88
1.220	957	7	5097	1.13	2518	1.50
1.321	577	4	4281	1.05	2148	1.35
1.425	370	3	3447	0.98	1817	1.22
1.650	153	3	2253	0.84	1279	1.00
2.028	35	1	1006	0.67	616	0.77

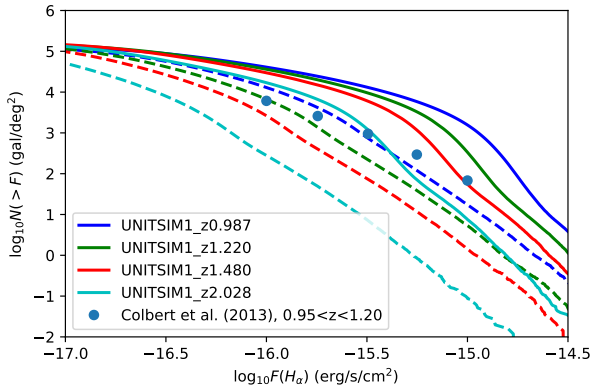


Figure 5. Cumulative counts per deg² as a function of H α flux (for a selection of redshifts) in comparison to the observational data of Colbert et al. (2013). The solid lines show un-attenuated fluxes while the dashed lines are for ELGs after applying our dust model (Section 2.3). Only results for UNITSIM1 (and for galaxies with $M_* > 10^9 M_\odot$) are shown.

this model as ‘RefMod’. We will construct two additional models (i.e. ‘PozMod1’ and ‘PozMod3’), but before we can define them we need to provide some more background information and go into the details of the work of Pozzetti et al. (2016, P16); by fitting to observed luminosity functions from existing H α surveys, P16 build three distinct models for their evolution. Different fitting methodologies, functional forms for the luminosity function, subsets of the empirical input data, and treatment of systematic errors were considered to explore the robustness of the results. Functional forms and model parameters were made available (and are being used here), along with the counts and redshift distributions up to $z \sim 2.5$ for a range of limiting fluxes bracketing the sensitivity of Euclid. Their models are named ‘Pozzetti model #1, #2, and #3’, with model #1 being considered the most optimistic and model #3 the most pessimistic for Euclid. The P16 models and the corresponding public data¹⁰ will later be used by us to generate distinct ELG catalogues different from aforementioned reference model ‘RefMod’.

We show in Fig. 6 the redshift evolution of the number density of our RefMod galaxies (i.e. applying a redshift-independent flux

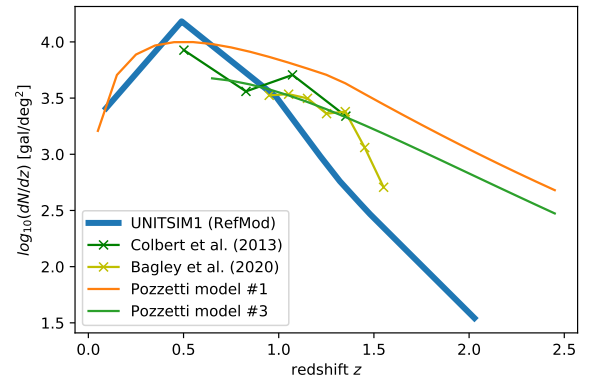


Figure 6. Redshift evolution of the number density of dust-attenuated ELGs for the RefMod (i.e. redshift-independent flux cut at 2×10^{-16} erg/s/cm²) in comparison to the observational data of Colbert et al. (2013) and Bagley et al. (2020). We also show model #1 and #3 of Pozzetti et al. (2016) for the same flux threshold (not to be confused with our own models PozMod1 and PozMod3 that were designed to match these number densities). Only UNITSIM1 ELGs are shown for clarity.

threshold of $F_{\text{cut}} = 2 \times 10^{-16}$ erg/s/cm² to the dust-attenuated model ELGs) with the comparison to observational data of Colbert et al. (2013). We also show two of the three models of P16: we show model #1 (most optimistic) and #3 (most pessimistic), also for a flux cut of 2×10^{-16} erg/s/cm². We can see how for $z < 1$ our ‘RefMod’ ELGs follow the same trends as the P16 models, but show a substantial lack of objects at higher redshift. Such a discrepancy between semi-analytic galaxies and the P16 models can already be seen in fig. 5 of P16, where their three models are compared against the results from two other SAMs. It should also be mentioned that a more recent study of the observed number density evolution of H α ELGs indicates a possible decline beyond redshift $z \sim 1.4$ (Bagley et al. 2020, lower right panel of fig. 7), although it is not as pronounced as the dip found for our SAGE ELGs. To highlight this we have added those data points¹¹ to our plot; while there is agreement with

¹⁰ The P16 data can be downloaded from here: <http://www.bo.astro.it/~pozzetti/Halpha/Halpha.html>

¹¹ The Bagley et al. (2020) data are based upon completeness-corrected measurements of the blended H α and NII fluxes, while our fluxes include only H α . We have therefore ‘corrected’ the Bagley et al. (2020) data points – as obtained with PlotDigitizer – by reversing their adjustment to model #3 of P16 to account for the combined fluxes. This was done by finding the shift needed to bring the digitized data points into the same kind of agreement with

model #3 in the redshift range $z \in [1, 1.5]$, the observational data drops even stronger for higher redshifts. This seems to indicate that even the most pessimistic model #3 of P16 overpredicts high- z ELGs. However, Bagley et al. (2020) also say that their higher redshift points are in the region where the sensitivity of their instrument could be degraded.

This discrepancy between our SAGE and the Pozzetti ELG number densities is also reflected in Table 1 where we list as a function of redshift the number density of ELGs in our reference model RefMod (as averaged over the four UNIT simulations, also providing the standard deviation). In order to overcome this deficit of ELGs at high redshift, we have constructed two additional ELG catalogues that are based on the data for the P16 models #1 and #3. Taking the Pozzetti predictions as a reference, we adjusted the flux thresholds applied to our model ELGs at each redshift so that we match the number densities of the two Pozzetti models #1 and #3, respectively. The resulting values are also provided in Table 1 in the columns with the headings ‘PozMod1’ and ‘PozMod3’, respectively; for a fixed redshift, we vary the flux threshold F_{cut} when selecting our UNITSIM ELGs until we reach that particular number density as reported by P16. Note that the Pozzetti et al. predictions are for the Euclid reference flux cut of $F_{\text{cut}} = 2 \times 10^{-16}$ erg/s/cm². We used this methodology with all four UNITSIM catalogues, and the means of the required flux cuts to our data are listed in the Table, too; we omit error estimates as they are below the reported accuracy. We are eventually left with three distinct ELG catalogues, all using the dust-attenuated fluxes:

RefMod: flux threshold of $F_{\text{cut}} = 2 \times 10^{-16}$ erg/s/cm² across all redshifts,

PozMod1: variable flux threshold to match the number density of Pozzetti’s model #1 at each redshift,

PozMod3: variable flux threshold to match the number density of Pozzetti’s model #3 at each redshift.

We emphasize that both PozMod1 and PozMod3 are *not* the two models #1 and #3 of P16. They are our own models where we adjusted the number densities to match those of model #1 and #3 of Pozzetti, respectively. We did this to correct for the lack of SAGE ELGs with respect to the Pozzetti models seen in Fig. 6.

As mentioned in the Introduction, Zhai et al. (2019) also made predictions for the number counts and its redshift evolution of H α -emitting galaxies based upon theoretically modelled galaxies found in UNITSIM1. But the fact that their galaxy abundances are in better agreement with observations (cf. their figs.3 and 4) stems from the fact that the number densities of their model ELGs, based upon the SAM GALACTICUS, were calibrated to the observed H α luminosity functions in the redshift range $z \in [0.8, 2.3]$.

Given the results presented in this section we conclude that our (dust-attenuated) UNITSIM-SAGE-ELGs will provide a fair sample and can be used for further analysis. And as a particular application we employ them for a study of galaxy clustering and the related bias.

5 CLUSTERING OF ELGS

Quantifying the clustering of galaxies is one of the main objectives of ongoing and upcoming galaxy surveys such as the Euclid satellite mission. Clustering measurements probe the fluctuations of the

the original Pozzetti model #3, as seen in the lower right panel of Bagley’s fig. 7 for the blended Pozzetti model #3.

underlying dark matter from the positions of galaxies, and they encode geometric model-dependent cosmological information. Using the positions of our theoretical UNITSIM ELGs, we now study the two-point correlation function $\xi_{\text{ELGs}}(r)$ and its redshift evolution. We further use the positions of 10^7 randomly selected dark matter particles from the total 4096^3 particles present in each of the UNIT gravity-only simulations to calculate $\xi_{\text{DM}}(r)$.¹² This allows us to also infer the bias that we define here as

$$b(r) = \sqrt{\frac{\xi_{\text{ELGs}}(r)}{\xi_{\text{DM}}(r)}} \quad (11)$$

between both populations and study its evolution with redshift, too. All two-point correlation functions (2PCFs) have been obtained with the CUTE¹³ software presented in Alonso (2012). In addition, for the results that we will present throughout this section, we have taken the average of the values computed for the 2PCF over the four simulations U1, U1IP, U2, and U2IP.

In the top panel of Fig. 7 we present the 2PCF computed for the RefMod ELGs (dashed lines) and dark matter (solid lines). The lower panel of the same figure shows the bias $b(r)$ defined via Eq. (11). In order to better verify the scale-dependence of the bias, we also calculate the ‘average’ bias

$$\langle b \rangle = \frac{1}{N_{\text{bin}} - 1} \sum_2^{N_{\text{bin}}} b_i, \quad (12)$$

where N_{bin} is the number of bins and $b_i = b(r_i)$ the value of the bias in distance bin r_i . This average bias $\langle b \rangle$ is shown as a dashed horizontal line in the lower panel, too. Note that we exclude the first bin in this calculation since for such small distances the bias is certainly scale-dependent (see Fig. 10 below). And it is obvious that the data for this particular model become rather noisy at high redshifts due to the very low number of objects above the reference flux cut of $F_{\text{cut}} = 2 \times 10^{-16}$ erg/s/cm² (see Table 1). But we can nevertheless appreciate that for distances $r \gtrsim 5h^{-1}$ Mpc the bias is remarkably constant, something we will quantify in more detail below.

An equivalent analysis has been conducted for our PozMod1 and PozMod3 ELGs, but we decided to only show here in Fig. 8 the results for the bias. Once more we can see how due to the reduced number of galaxies at redshift $z = 2.028$ we get fairly noisy results. But the most important point is that the bias of ELGs in both models remains constant on scales $r > 5h^{-1}$ Mpc. Below this scale it is obvious that the mixture contribution between the one- and two-halo terms will introduce non-linear effects which in turn will cause the bias to no longer behave independently with scale. We further note that the bias clearly is a function of redshift. But this is also expected, as the mass of the haloes hosting ELGs will change with redshift, too (see Fig. A2 in the Appendix). Not only that, but haloes of the same mass at different redshifts will also have a different bias. It therefore only appears natural that bias increases with redshift; if something formed at all at high redshift, it already means it is ‘biased’, but the size of this increase still remains to be quantified.

Fig. 9 now quantifies the evolution of the average bias $\langle b \rangle$ (obtained from the results presented in Fig. 7 and Fig. 8) as a function of redshift for our three models RefMod, PozMod1, and PozMod3. This figure is accompanied by Table 2 that lists the plotted values. We find that for all our models – also for the ones where we matched the number

¹² We confirm that the resulting 2PCFs have converged and will not change when using more particles. Further, this number of dark matter particles is comparable to the number of ELGs, at least at redshifts $z \leq 1$.

¹³ <https://github.com/damonge/CUTE>

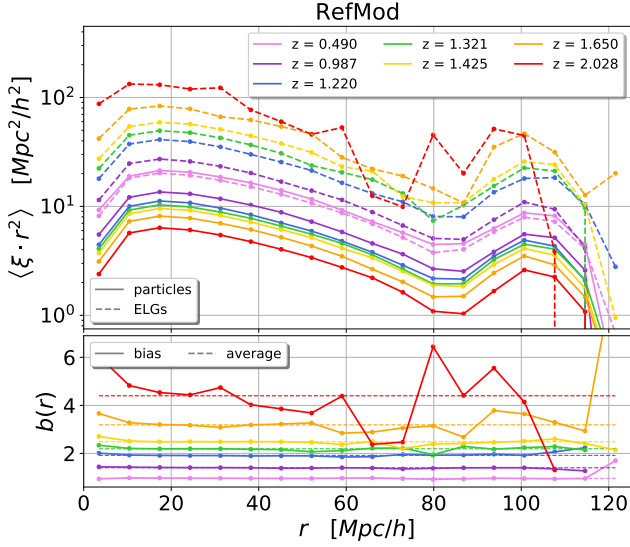


Figure 7. Top panel: 2PCF of SAGE ELGs with flux greater than 2×10^{-16} erg/s/cm² (RefMod model, dashed lines) and collisionless trace particles (solid lines) for various redshifts. Bottom panel: associated bias as defined by Eq. (11).

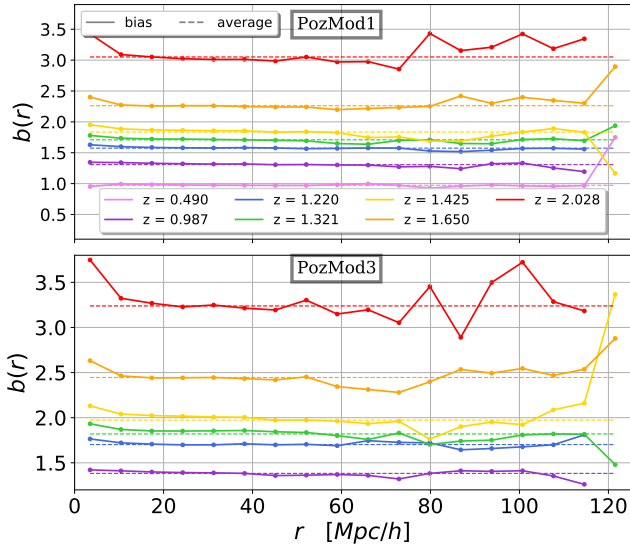


Figure 8. The bias for the PozMod1 (upper panel) and PozMod3 (lower panel) models using the same r -range as for Fig. 7.

Table 2. Bias values averaged for scales larger than $5h^{-1}$ Mpc computed for the three models of interest (RefMod, PozMod1, PozMod3) corresponding to the dashed lines presented in the three bias panels of Fig. 8.

z	RefMod	PozMod1	PozMod3
0.490	0.96	0.97	-
0.987	1.4	1.31	1.38
1.220	1.92	1.57	1.7
1.321	2.19	1.71	1.82
1.425	2.48	1.83	1.97
1.650	3.19	2.26	2.45
2.028	4.4	3.05	3.24

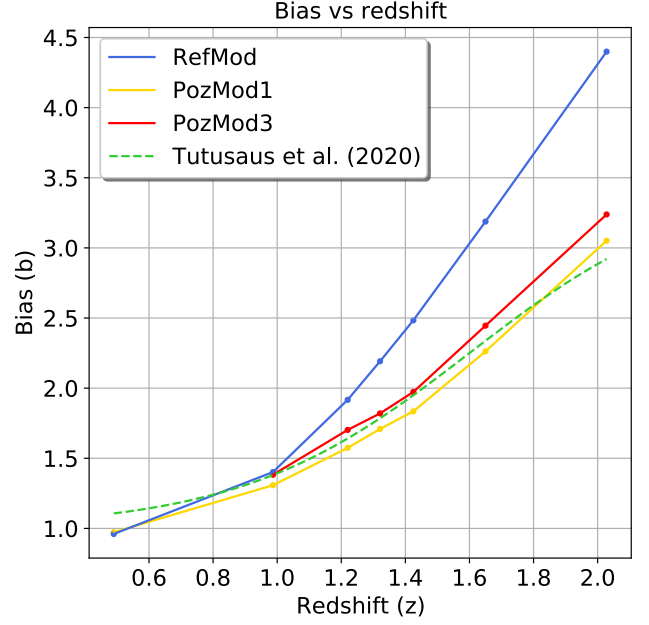


Figure 9. Bias values averaged for scales larger than $5h^{-1}$ Mpc computed for the three models of interest (RefMod - blue, PozMod1 - yellow, PozMod3 - red). The green dashed line is the best fit $b(z)$ for the bias found in Euclid’s *Flagship* simulation (Tutusaus et al. 2020).

densities to the P16 predictions – the bias systematically increases with redshift. And the strength of this relation for our PozMod1 and PozMod3 models is further in excellent agreement with the relation presented in Tutusaus et al. (2020, eq. 11), shown by the dashed line in the Fig. 9. The $b(z)$ function given in Tutusaus et al. is derived from studying the bias in the Euclid *Flagship* simulation.¹⁴ The *Flagship* simulation is also just based upon dark matter, but the population of their dark matter haloes with galaxies is quite distinct to our approach: they have applied a Halo Occupation Distribution (HOD) that does not take into account the merger trees of the haloes (for a comparison of these two different techniques see, for instance, Knebe et al. 2015, 2018b).¹⁵ Merson et al. (2019) also forecast the linear bias for H α -emitting galaxies at these redshift. They also used the HOD for which they calibrated the dust attenuation to reproduce observed H α counts. Their $b(z)$ though deviates from our predictions: their values are systematically lower, e.g. of order 25 per cent at $z \approx 1$ increasing to ca. 40 per cent lower at $z \approx 2$. We finally remark that our findings for the redshift evolution of the bias $b(z)$ are also in agreement with those of Favole et al. (2017, right panel of fig. 6). However, in their work, the bias increases more mildly, as the SDSS redshift range studied there is very much reduced compared to ours.

One might now argue that the findings presented here are sensitive to the particulars of the dust attenuation model. However, this objection primarily applies to our RefMod model. For the other two models there exists a degeneracy between the attenuation calculation (esp. Eq. (7)) and the way PozMod1 and PozMod3 were constructed:

¹⁴ https://www.euclid-ec.org/?page_id=4133

¹⁵ While there is no reference paper for this galaxy catalogue, we nevertheless like to mention that it is based upon the MICE HOD (Carretero et al. 2015). The clustering is fit to SDSS galaxies as a function of magnitude and colour at low redshift. Then, most of the properties are assumed to depend on redshift only via their SEDs/color evolution, allowing for correlations between many observables.

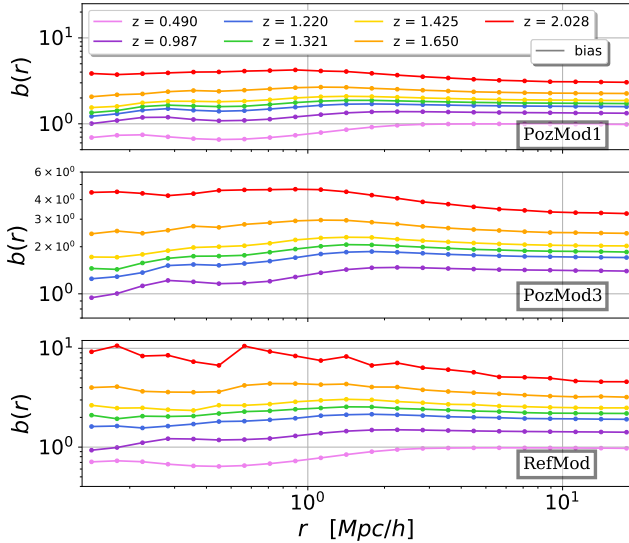


Figure 10. The bias $b(r)$ in logarithmic r bins, focusing on the small scales up to $r < 20h^{-1}\text{Mpc}$. The upper panel shows the RefMod model, the middle one PozMod1, and the lower panel PozMod3.

the flux threshold at each redshift was chosen to reproduce the number density as provided by P16. This can be verified below in Section A3 where we show the analogy to Fig. 9, but using the non-attenuated ELGs.

So far we have mainly focused on large scales, but to conclude this section we also present how the bias varies for *small* scales. In Fig. 10 we present the bias $b(z)$ for various redshifts and all our three models out to $r \approx 20h^{-1}\text{Mpc}$ using logarithmic binning. We observe that for redshifts $z < 2$ the bias remains constant down to scales $r \approx 3h^{-1}\text{Mpc}$ and then starts to mildly drop. It is actually around this distance that we expect the contribution from the one-halo term to start to become relevant. However, this behaviour weakens for higher redshifts and possibly reverses for $z = 2$. Something similar has also been observed by Nuza et al. (2012, fig. 10) for BOSS CMASS galaxies, but there the inversion was already seen at redshift $z \approx 0.53$ (and one needs to bear in mind that CMASS galaxies and ELGs are not directly comparable as they are different types of galaxies, where the latter are mostly star-forming and the former could be dominated by passive galaxies).

6 CONCLUSIONS

Realistic simulations are a necessary tool in order to optimise and validate the methodology that will be used to extract cosmological constraints from future surveys. Indeed, they are used to estimate the theoretical error budget on surveys (for example, for the eBOSS-ELG analysis see Alam et al. 2020). In this work we have employed the UNIT simulations, which model the evolution of dark matter within a $1h^{-1}\text{Gpc}$ box at a mass resolution of $1.2 \times 10^9 h^{-1} M_{\odot}$ per particle (Chuang et al. 2019). Given the large volume of these simulations together with the fixed-and-paired technique of Angulo & Pontzen (2016) that enhances the effective volume of the simulations, the resulting galaxy mocks that we have produced represent a unique resource for model testing based on SAM of galaxy formation. We used our ELG catalogues to make predictions for the galaxy statistics that the Euclid experiment is expected to obtain for redshifts between

$0.9 < z < 1.8$. Note that the simulations presented here cover an effective survey volume of about seven times the effective survey volume of Euclid (Chuang et al. 2019). Also, having the galactic physics included is key, since the complicated relation between haloes and galaxies can modify the clustering of ELGs significantly, even at scales used to put cosmological constraints when working in Fourier space (see, for instance, Gonzalez-Perez et al. 2020; Avila et al. 2020).

For this work we have generated four synthetic catalogues of emission-line galaxies. The galaxies were first obtained by applying the semi-analytic galaxy formation model SAGE (Croton et al. 2016) to the gravity-only UNIT simulations. They were then subjected to the emission line modelling with the GET_EMLINES code (Orsi et al. 2014) and – following Favole et al. (2019) – an additional dust attenuation model. As argued throughout Section 3, the properties associated with our UNITSIM galaxies appear to reproduce the behaviour observed for real galaxies in the range of redshifts $0 \leq z < 2$, where our validation focused on the properties most relevant for the construction of ELGs. In Section 4 we adjusted the number densities of our UNITSIM ELGs in various ways by applying distinct flux thresholds to them, eventually comparing the redshift evolution of their abundance to observations. When studying the density of galaxies per deg^2 with fluxes greater than $2 \times 10^{-16} \text{ erg/s/cm}^2$ as a function of redshift we observe that the density obtained for the UNITSIM ELGs might underestimate the expected density of galaxies observed from redshift $z \sim 1.4$ onwards. Nevertheless, the most recent study by Bagley et al. (2020) suggests that the observational value for this quantity could be closer to our results. Therefore, the number densities predicted by P16 could give overestimated galaxy densities at high redshifts.

We study the clustering of three different samples listed in Table 1: one with the Euclid flux cut applied and two in which the flux cuts are adjusted to follow the predictions by two of the models in P16. We measure the linear bias as a function of redshift by averaging $\xi_{\text{ELGs}}/\xi_{\text{DM}}$ for scales $r > 5 \text{ Mpc}$. For the samples whose abundance is matched to P16 samples we find a $b(z)$ in line with the findings reported in Tutusaus et al. (2020) for the Euclid *Flagship* simulation. This is striking since the *Flagship* mock was constructed following a very different methodology (Carretero et al. 2015). The linear bias is a key parameter to understand the cosmological power of Euclid and can help construct forecasts that inform the optimisation of both observational and analysis strategies. The linear bias of $\text{H}\alpha$ galaxies may be particularly relevant for forecasts on studies such as primordial non-Gaussianities or relativistic effects. Additionally, we report the clustering at small scales, that becomes scale-dependent: these measurements can be used to test the robustness of different large-scale structure models to extract cosmological information from the small scales, that have the highest signal-to-noise ratio but at the same time are the most difficult to model.

One might argue that an improved and possibly even redshift-dependent dust attenuation modelling (as, for instance, used in Zhai et al. 2019) might change our results. While this would certainly have an effect on our reference model RefMod, we do not expect to find a big impact on the findings for PozMod1 and PozMod3. These latter models were constructed such as to reproduce the number counts predicted by P16, which is degenerate with the dust attenuation; while the dust model will shift number density counts (cf. Fig. 5), this will be countered by the subsequent re-normalisation when matching Pozzetti et al. (see Fig. A3).

We like to close with the remark that all galaxy catalogues and the ELG properties used in this work have been made publicly available

to the community at the <http://www.unitsims.org> website. They can be used for a great variety of studies and have extensive applications like, for example, informing Halo Occupation Distribution models: we will study the properties of $H\alpha$ ELG HOD models in a follow-up paper.

ACKNOWLEDGEMENTS

AK and GY are supported by the MICIU/FEDER through grant number PGC2018-094975-C21. AK further thanks Chasing Dorothea for all i want. SA is supported by the MICUES project, funded by the EU H2020 Marie Skłodowska-Curie Actions grant agreement no. 713366 (InterTalentum UAM). DLC acknowledge the support of the ERC-StG number 716151 (BACCO). GF acknowledges financial support from the SNF 175751 “Cosmology with 3D Maps of the Universe” research grant. VGP is supported by the Atracción de Talento Contract no. 2019-T1/TIC-12702 granted by the Comunidad de Madrid in Spain. ARHS acknowledges receipt of the Jim Buckee Fellowship at ICRAR-UWA. FSK acknowledges financial support from the Spanish Ministry of Economy and Competitiveness (MINECO) under the Severo Ochoa program SEV-2015-0548, and for the grants RYC2015-18693 and AYA2017-89891-P. GR is grateful for the financial support granted by the Ministry of Education of Spain (FPI, MEC) with reference PRE2018-087035, for the I+D project with reference to SEV -2016-0597 - 18-2 IFT (UAM-CSIC)

The UNIT simulations have been produced in the MareNostrum Supercomputer, hosted by the Barcelona Supercomputing Center, Spain, under the PRACE project number 2016163937.

This research has made use of NASA’s Astrophysics Data System and the arXiv preprint server. This work was created by making use of the following software: PYTHON, MATPLOTLIB (Hunter 2007), NUMPY (van der Walt et al. 2011), SCIPY (Virtanen et al. 2019), and ASTROPY (Astropy Collaboration et al. 2013, 2018).

DATA AVAILABILITY

The data is available at <http://www.unitsims.org>. There one finds the halo catalogues and merger tree of the underlying dark matter-only simulations, and the SAGE galaxies alongside their emission-line information.

The data is directly available for those redshifts used in this paper; for other redshifts the data will be available upon request.

REFERENCES

- Abbott T. M. C., et al., 2018, *The Astrophysical Journal Supplement Series*, 239, 18
- Alam S., et al., 2017, *MNRAS*, 470, 2617
- Alam S., et al., 2020, arXiv e-prints, p. arXiv:2007.09004
- Allen M. G., Groves B. A., Dopita M. A., Sutherland R. S., Kewley L. J., 2008, *The Astrophysical Journal Supplement Series*, 178, 20–55
- Alonso D., 2012, preprint, (arXiv:1210.1833)
- Amendola L., et al., 2013, *Living Reviews in Relativity*, 16
- Angulo R. E., Pontzen A., 2016, *Monthly Notices of the Royal Astronomical Society: Letters*, 462, L1–L5
- Asplund M., Grevesse N., Sauval A. J., Scott P., 2009, *ARA&A*, 47, 481
- Asquith R., et al., 2018, *Monthly Notices of the Royal Astronomical Society*, 480, 1197
- Astropy Collaboration et al., 2013, *A&A*, 558, A33
- Astropy Collaboration et al., 2018, *AJ*, 156, 123
- Avila S., et al., 2020, *MNRAS*, 499, 5486
- Bagley M. B., et al., 2020, *ApJ*, 897, 98
- Baldry I. K., Glazebrook K., Driver S. P., 2008, *MNRAS*, 388, 945
- Behroozi P. S., Wechsler R. H., Wu H.-Y., 2012, *The Astrophysical Journal*, 762, 109
- Bellstedt S., et al., 2021, arXiv e-prints, p. arXiv:2102.11514
- Berlind A. A., et al., 2003, *ApJ*, 593, 1
- Cardelli J. A., Clayton G. C., Mathis J. S., 1989, *ApJ*, 345, 245
- Carretero J., Castander F. J., Gaztañaga E., Crocce M., Fosalba P., 2015, *MNRAS*, 447, 646
- Chuang C.-H., et al., 2019, *Monthly Notices of the Royal Astronomical Society*, 487, 48–59
- Colbert J. W., et al., 2013, *ApJ*, 779, 34
- Cole S., et al., 2005, *MNRAS*, 362, 505
- Collaboration D., et al., 2016, *The DESI Experiment Part I: Science, Targeting, and Survey Design* (arXiv:1611.00036)
- Croton D. J., et al., 2006, *MNRAS*, 365, 11
- Croton D. J., et al., 2016, *ApJS*, 222, 22
- Daddi E., et al., 2007, *ApJ*, 670, 156
- Davidzon I., et al., 2017, *A&A*, 605, A70
- Dawson K. S., et al., 2012, *The Astronomical Journal*, 145, 10
- Dawson K. S., et al., 2016, *The Astronomical Journal*, 151, 44
- De Barros S., Reddy N., Shivaei I., 2016, *ApJ*, 820, 96
- De Lucia G., Blaizot J., 2007, *MNRAS*, 375, 2
- Draine B. T., 2003, *Annual Review of Astronomy and Astrophysics*, 41, 241
- Drinkwater M. J., et al., 2010, *Monthly Notices of the Royal Astronomical Society*, 401, 1429–1452
- Eisenstein D. J., et al., 2005, *ApJ*, 633, 560
- Elbaz D., et al., 2011, *Astronomy & Astrophysics*, 533, A119
- Favole G., Rodríguez-Torres S. A., Comparat J., Prada F., Guo H., Klypin A., Montero-Dorta A. D., 2017, *MNRAS*, 472, 550
- Favole G., et al., 2019, arXiv e-prints, p. arXiv:1908.05626
- Ferland G. J., et al., 2013, *Rev. Mex. Astron. Astrofis.*, 49, 137
- Gonzalez-Perez V., et al., 2020, *MNRAS*, 498, 1852
- Groves B. A., Dopita M. A., Sutherland R. S., 2004, *The Astrophysical Journal Supplement Series*, 153, 75–91
- Hatton S., Devriendt J. E. G., Ninin S., Bouchet F. R., Guiderdoni B., Vibert D., 2003, *MNRAS*, 343, 75
- Hunter J. D., 2007, *Computing in Science & Engineering*, 9, 90
- Izquierdo-Villalba D., Bonoli S., Spinoso D., Rosas-Guevara Y., Henriques B. M. B., Hernández-Montenegro C., 2019, *MNRAS*, 488, 609
- Kauffmann G., 1996, *MNRAS*, 281, 475
- Kennicutt Jr. R. C., 1989, *ApJ*, 344, 685
- Knebe A., et al., 2015, *MNRAS*, 451, 4029
- Knebe A., et al., 2018a, *MNRAS*, 474, 5206
- Knebe A., et al., 2018b, *MNRAS*, 475, 2936
- Laureijs R., et al., 2011, *Euclid Definition Study Report* (arXiv:1110.3193)
- Lee J., et al., 2020, arXiv e-prints, p. arXiv:2006.01039
- Merson A., Smith A., Benson A., Wang Y., Baugh C., 2019, *MNRAS*, 486, 5737
- Nuza S. E., Sanchez A. G., Prada F., Klypin A., Schlegel D. J., Gotober S., Montero-Dorta A. D., Manera M. e. a., 2012, preprint, (arXiv:1202.6057)
- Orsi A., Padilla N., Groves B., Cora S., Tecce T., Gargiulo I., Ruiz A., 2014, *Monthly Notices of the Royal Astronomical Society*, 443, 799–814
- Osterbrock D. E., 1989, *Astrophysics of gaseous nebulae and active galactic nuclei*
- Parkinson D., et al., 2012, *Phys. Rev. D*, 86, 103518
- Planck Collaboration et al., 2015, preprint, (arXiv:1502.01589)
- Pozzetti L., et al., 2016, *A&A*, 590, A3
- Scott N., Graham A. W., Schombert J., 2013, *ApJ*, 768, 76
- Sobral D., Stroe A., Koyama Y., Darvish B., Calhau J., Afonso A., Kodama T., Nakata F., 2016, *MNRAS*, 458, 3443
- Somerville R. S., Primack J. R., Faber S. M., 2001, *MNRAS*, 320, 504
- Spergel D., et al., 2013, *Wide-Field InfraRed Survey Telescope–Astrophysics Focused Telescope Assets WFIRST-AFTA Final Report* (arXiv:1305.5422)
- Spergel D., et al., 2015, *Wide-Field Infrared Survey Telescope–Astrophysics Focused Telescope Assets WFIRST-AFTA 2015 Report* (arXiv:1503.03757)
- Springel V., Yoshida N., White S. D., 2001, *New Astronomy*, 6, 79–117
- Stark D. V., McGaugh S. S., Swaters R. A., 2009, *AJ*, 138, 392
- The Dark Energy Survey Collaboration 2005, arXiv e-prints, pp astro-ph/0510346
- Tremonti C. A., et al., 2004, *ApJ*, 613, 898
- Tutusaus I., et al., 2020, arXiv e-prints, p. arXiv:2005.00055
- Vale A., Ostriker J. P., 2004, *MNRAS*, 353, 189
- Virtanen P., et al., 2019, arXiv e-prints, p. arXiv:1907.10121
- White S. D. M., Frenk C. S., 1991, *ApJ*, 379, 52
- Yang L., Roberts-Borsani G., Treu T., Birrer S., Morishita T., Bradač M., 2021, *MNRAS*, 501, 1028
- York D. G., et al., 2000, *AJ*, 120, 1579
- Zhai Z., Benson A., Wang Y., Yepes G., Chuang C.-H., 2019, *Monthly Notices of the Royal Astronomical Society*, 490, 3667–3678
- Zhai Z., Chuang C.-H., Wang Y., Benson A., Yepes G., 2021, *MNRAS*, 501, 3490
- de Jong R. S., et al., 2012, *Ground-based and Airborne Instrumentation for Astronomy IV*
- eBOSS Collaboration et al., 2020, arXiv e-prints, p. arXiv:2007.08991
- van der Walt S., Colbert S. C., Varoquaux G., 2011, *Computing in Science Engineering*, 13, 22

APPENDIX A: ADDITIONAL VALIDATION PLOTS

In this Appendix we provide supplementary plots that further show the validity and properties of the SAGE (ELG) galaxies used throughout this study.

A1 Stellar Mass Function of flux selected ELGs

In order to view the effect of the flux selection and its relation to the stellar masses of the resulting sub-sample of ELGs, we show in Fig. A1 both the SMF of all ELGs (i.e. no flux cut, dashed lines) and the ELGs for various redshifts. We appreciate that the majority of ELGs coincide with the most massive galaxies.

A2 Halo Mass Function of flux selected ELGs

As our post-processing will eventually lead to selecting a sub-sample of the underlying dark matter haloes, we show here the mass function of the haloes hosting our ELGs.

Table A1. Analog to Table 2, but using non-attenuated ELGs.

z	RefMod	PozMod1	PozMod3
0.490	0.94	0.94	-
0.987	1.18	1.23	1.28
1.220	1.35	1.44	1.48
1.321	1.43	1.54	1.58
1.425	1.52	1.66	1.7
1.650	1.76	1.89	2.0
2.028	2.19	2.42	2.55

Table A2. Analog to Table 1, but using non-attenuated ELGs: the two columns for each of our models PozMod1 and PozMod3 give the predicted number density of ELGs per square degree (taken from their Table 3) and the flux threshold (measured in 10^{-16} erg/s/cm²) required to match that number for our SAGE ELGs, as an average over all four UNIT simulations (the standard deviation is smaller than the reported accuracy).

z	PozMod1		PozMod3	
	dN/dz	$\langle F_{\text{cut}} \rangle$	dN/dz	$\langle F_{\text{cut}} \rangle$
0.490	9946	6.441	-	-
0.987	7353	4.864	3779	7.080
1.220	5097	4.600	2518	6.200
1.321	4281	4.452	2148	5.759
1.425	3447	4.343	1817	5.353
1.650	2253	3.930	1279	4.564
2.028	1006	3.330	616	3.687

A3 Bias for non-attenuated ELGs

Here we provide the analogue to Fig. 9, but using the non-attenuated ELGs. As expected, the main difference is found for the RefMod model, which uses a redshift-independent flux threshold. For our two models PozMod1 and PozMod3 we only observe a mild change in the direction of finding a marginally lower bias when using non-attenuated fluxes. This can be verified in Table A1, which provides the numbers entering Fig. A3. We find that the bias is marginally smaller at higher redshift for these non-attenuated models. Note that these the models used here were constructed following the same approach outlined in Section 4.2. We therefore also provide here the analog to Table 1: Table A2 shows the mean flux thresholds as a function of redshift for the same target dN/dz values as used before.

APPENDIX B: CONVERSION OF NUMBER DENSITIES

Here we show the steps necessary to go from volumetric number density

$$n = \frac{dN}{dV} \quad (\text{B1})$$

to the angular and redshift density

$$\eta = \frac{dN}{d\Omega dz} . \quad (\text{B2})$$

Taking into account

$$dV = d\Omega r^2 dr \quad (\text{B3})$$

where $d\Omega$ is the solid angle in stereoradians, we then get

$$\eta = n \cdot r^2 \frac{dr}{dz} . \quad (\text{B4})$$

Therefore, to go from number density $n = N/V$ of galaxies to number density of galaxies per square-degree and redshift interval, i.e. dN/dz , we find

$$\frac{dN}{dz} = n r^2(z) \frac{dr}{dz} \left(\frac{\pi}{180^\circ} \right)^2 , \quad (\text{B5})$$

where dN/dz is measured in galaxies per deg² and $r(z)$ the comoving distance

$$r(z) = \frac{c}{H_0} \int_0^z \frac{ds}{E(s)} \quad (\text{B6})$$

with

$$E^2(z) = \frac{1}{(\Omega_{r,0}(1+z)^4 + \Omega_{m,0}(1+z)^3 + \Omega_{k,0}(1+z)^2 + \Omega_{\Lambda,0})} , \quad (\text{B7})$$

where Ω_X are the usual density parameters of radiation ($X = r$), matter ($X = m$), curvature ($X = k$), and cosmological constant ($X = \Lambda$) at present time. We note that the derivative of R with respect to z as needed in Eq. (B5) is simply

$$\frac{dr}{dz} = \frac{c}{H_0} \frac{1}{E(z)} . \quad (\text{B8})$$

This paper has been typeset from a $\text{\TeX}/\text{\LaTeX}$ file prepared by the author.

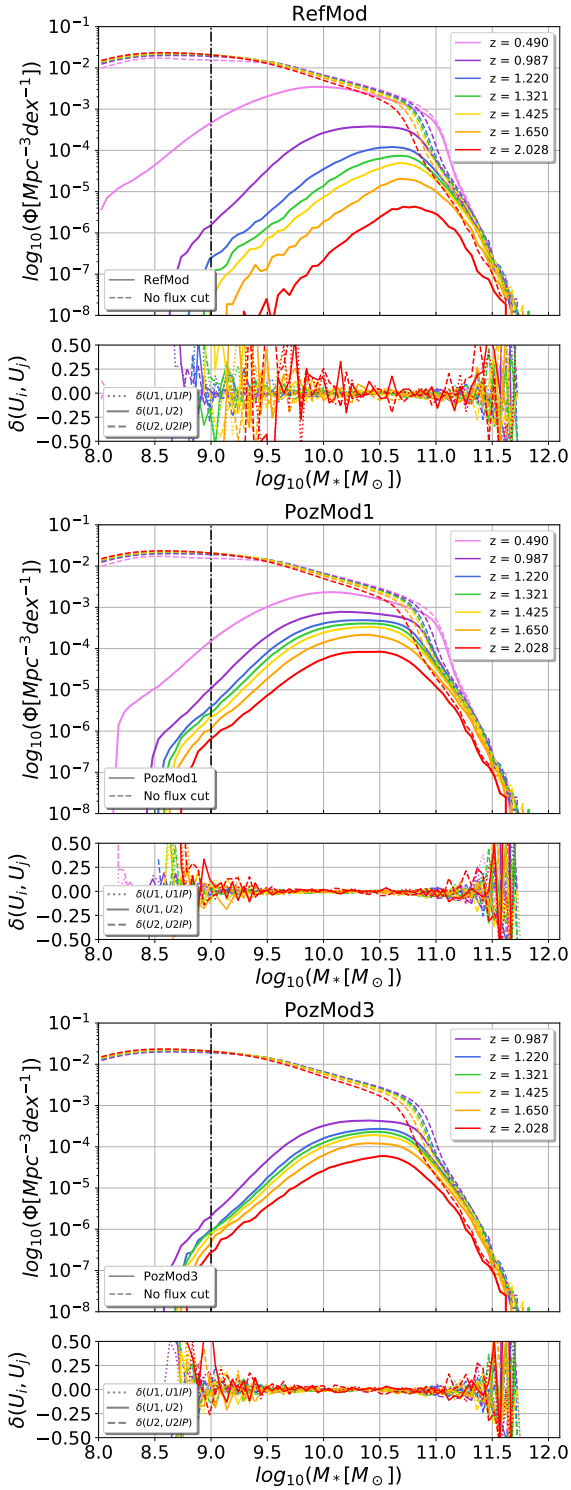


Figure A1. Stellar mass function of all ELGs (dashed lines) and the flux-selected samples (solid lines) for RefMod (upper panel), PozMod1 (middle panel), and PozMod3 (lower panel). The vertical dot-dashed line shows our lower stellar mass limit.

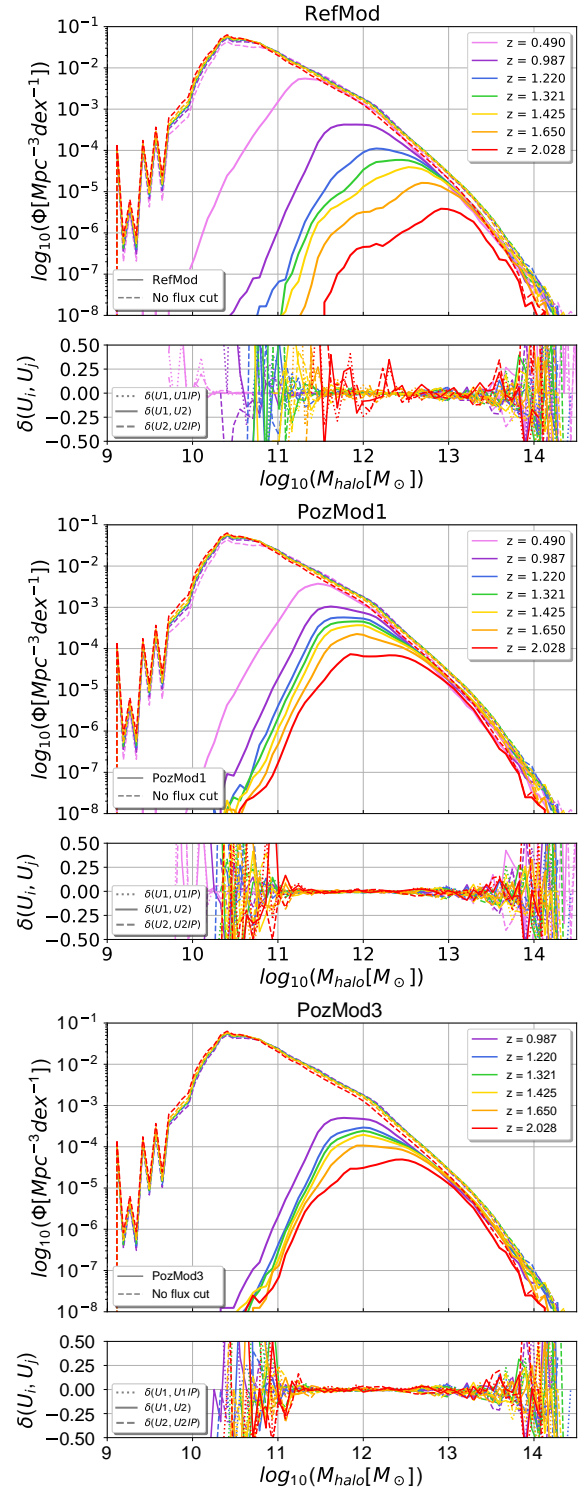


Figure A2. Halo mass function of all ELGs (dashed lines) and the flux-selected samples (solid lines) for RefMod (upper panel), PozMod1 (middle panel), and PozMod3 (lower panel).

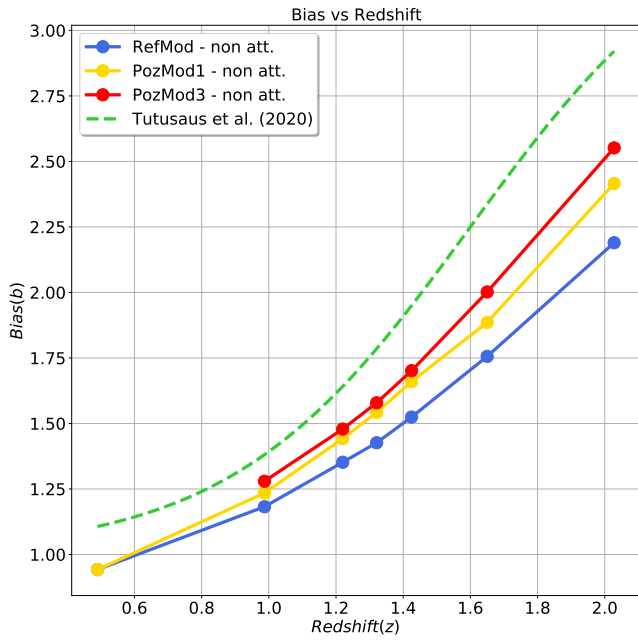


Figure A3. Redshift evolution of the bias for non-attenuated ELGs.